PHYSICAL REVIEW APPLIED **14,** 064044 (2020)

Antireflection and Wavefront Manipulation with Cascaded Metasurfaces

Fengyuan Yang,[1] Brian O. Raeker,[2] Dat T. Nguyen,[3] Joseph D. Miller,[3] Ze Xiong,[1]
Anthony Grbic,[2,*] and John S. Ho[1,4,5,†]

[1] *Department of Electrical and Computer Engineering, National University of Singapore, Singapore 117583, Singapore*
[2] *Department of Electrical Engineering and Computer Science, University of Michigan, Ann Arbor, Michigan 48109-2122, USA*
[3] *NUS Graduate School for Integrative Sciences and Engineering, National University of Singapore, Singapore 119077, Singapore*
[4] *The N.1 Institute for Health, National University of Singapore, Singapore 117456, Singapore*
[5] *Institute for Health Innovation and Technology, National University of Singapore, Singapore 117599, Singapore*

(Received 5 September 2020; revised 4 November 2020; accepted 18 November 2020; published 14 December 2020)

Layered structures are widely used in optics to control wave reflection and propagation at interfaces but their thickness relative to the wavelength hinders their application in the radio-frequency regime. Here, we design and experimentally demonstrate cascaded metasurfaces with deeply subwavelength thickness that provide both antireflection and wavefront manipulation. We describe the systematic synthesis of the metasurface layers from a prescribed scattering response and demonstrate designs capable of providing near-perfect microwave transmission through glass as well as antireflection focusing of wireless signals from air into water.

DOI: 10.1103/PhysRevApplied.14.064044

I. INTRODUCTION

The control of electromagnetic waves at the interface between two media is important for many radio-frequency technologies [1–3]. In particular, the ability to both suppress reflection and manipulate wavefronts at interfaces between air and materials can, among other applications, enhance wireless-signal transmission through obstacles [4], permit radar imaging of underground objects [5], and enable wireless power transfer to implanted medical devices [6,7]. In optics, the standard approach to suppressing reflection is to use layered antireflection films, which generate destructive interference between the reflected waves via phase delays accumulated through the layers [8]. However, because the film thicknesses are necessarily comparable to the wavelength, their application at radio frequencies is limited due to their physically thick dimensions. This limitation also presents a challenge for wavefront manipulation, as it precludes the use of lenses, reflectors, and other components that also rely on the propagation phase.

Metasurfaces provide unprecedented capabilities in manipulating electromagnetic waves across deeply subwavelength layers. Examples include generalization of Snell's law [9], asymmetric transmission [10], and polarization rotation [11,12]. Although recent work has demonstrated highly transmissive metasurfaces in free space [13, 14], their design and application at the interface between two media has been relatively less explored. For example, antireflection metasurfaces based on two thin layers of scatterers [15] have been employed for reflectionless transmission of radio-frequency waves from air into concrete [16] and into biological tissue [17]. These designs, however, do not provide capabilities in wavefront manipulation and are not straightforwardly modified without incurring reflection. A general approach to achieve reflectionless wavefront control is to introduce bianisotropy—coupling between the electric and magnetic response—in order to transform the transverse impedance of the incident wave [18–20]. Through the use of this approach, bianisotropic metasurfaces based on wire-loop inclusions and multilayer structures have been shown to provide wavefront manipulation with high-efficiency transmission in free space [19–23]. Furthermore, bianisotropic metasurfaces that eliminate reflection at the interface between two different media have also been previously demonstrated, although without capabilities in wavefront manipulation [24]. While metasurfaces that combine these functionalities have been proposed [25–27], they have yet to be experimentally demonstrated, in part due to challenges in the design of the unit cells. To

---

[*] agrbic@umich.edu
[†] johnho@nus.edu.sg

© 2020 American Physical Society

simultaneously control the wavefront and suppress reflection from the interface, a systematic process is needed to design unit cells that implement independent transformations of the impedance and phase of the incident wave.

Here, we systematically design and experimentally demonstrate metasurfaces capable of antireflection and wavefront manipulation at the interface between two different media. The metasurfaces comprise multiple cascaded layers of patterned metallic claddings, which generate a prescribed bianisotropic response when cascaded over a deeply subwavelength distance [28]. Using wave-matrix analysis [28], we obtain closed-form expressions for the sheet admittances of the individual layers and then realize the sheet admittances using interdigitated capacitive and H-shaped inductive unit-cell structures. We validate the design process by developing a thin ($<\lambda/25$, where λ is the wavelength in air) antireflection metasurface for the interface between air and glass (a 6.5-fold difference in permittivity) at 2.4 GHz, corresponding to the industrial, scientific, and medical frequency band (which includes Wi-Fi and Bluetooth). We then use our approach to design and demonstrate a metasurface capable of focusing a normally incident wave from air into water (a 78-fold difference in permittivity) without reflection. The versatility of these metasurfaces in controlling waves at interfaces with arbitrary materials opens up a wide range of opportunities for wireless communication, biomedical devices, and wireless power transfer.

II. CASCADED-METASURFACE DESIGN

A. Design process

We begin by considering a plane wave incident on an interface between two different media [Fig. 1(a)]. The transverse-electric (TE) field components of the positive-propagating $\mathbf{E}_i^+$ and negative-propagating $\mathbf{E}_i^-$ waves in media i are related as follows:

$$\begin{pmatrix} \mathbf{E}_1^- \\ \mathbf{E}_2^+ \end{pmatrix} = \begin{pmatrix} \mathbf{S}_{11} & \mathbf{S}_{12} \\ \mathbf{S}_{21} & \mathbf{S}_{22} \end{pmatrix} \begin{pmatrix} \mathbf{E}_1^+ \\ \mathbf{E}_2^- \end{pmatrix}, \tag{1}$$

where $\mathbf{S}_{ij}$ are the 2×2 scattering parameters (S parameters) in the Jones-matrix form. The design of the metasurface involves determining a flat structure that realizes $\mathbf{S}_{ij}$ when placed on the interface. To achieve antireflection, the diagonal elements are required to vanish: $\mathbf{S}_{11} = \mathbf{S}_{22} = \mathbf{0}$. Conservation of local power flux requires that the corresponding transmission coefficients satisfy

$$\mathbf{S}_{21} = \sqrt{\eta_2/\eta_1}\, e^{j\varphi}\mathbf{I}, \quad \mathbf{S}_{12} = \sqrt{\eta_1/\eta_2}\, e^{j\varphi}\mathbf{I}, \tag{2}$$

where η_i is the transverse-wave impedance of the waves in each region, $\mathbf{I}$ the 2×2 identity matrix, and φ is an arbitrary phase shift across the interface. In nonmagnetic media, we have $\eta_i|_{\text{TE}} = \eta_0/(\sqrt{\varepsilon_i}\cos\theta)$ for a TE wave or $\eta_i|_{\text{TM}} = \eta_0 \cos\theta/\sqrt{\varepsilon_i}$ for a transverse-magnetic (TM) wave, where η_0 is the vacuum wave impedance, ε_i the relative permittivity for the ith medium, and θ is the angle of incidence normal to the interface. Such a reflectionless metasurface can also manipulate the wavefront by imposing a spatially varying transmission phase φ [9,18].

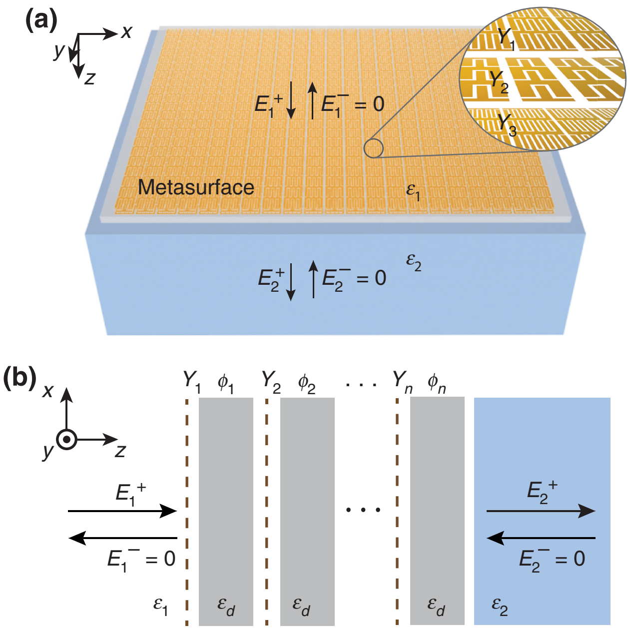

FIG. 1. Cascaded metasurfaces for antireflection and wavefront manipulation. (a) An illustration of a three-layer cascaded metasurface placed on the interface between two media. (b) A model for the transmission through the cascaded n-layer metasurface.

Cascaded metasurfaces allow reciprocal scattering parameters to be systematically realized using multiple patterned metallic claddings separated by subwavelength dielectric spacers [10,11,18,20,25,28–30]. To facilitate the calculation of wave propagation across the layers, the desired scattering parameters are converted to the wave matrix $\mathbb{M}$ [28]:

$$\mathbb{M} = \begin{pmatrix} \mathbf{I} & \mathbf{0} \\ \mathbf{S}_{11} & \mathbf{S}_{12} \end{pmatrix} \begin{pmatrix} \mathbf{S}_{21} & \mathbf{S}_{22} \\ \mathbf{0} & \mathbf{I} \end{pmatrix}^{-1}. \tag{3}$$

$\mathbb{M}$ is a 4×4 matrix that directly relates the transverse field components of the incident and transmitted electric fields at one port to those at the other. It can be decomposed as the product of wave matrices across n layers, as

$$\begin{pmatrix} \mathbf{E}_1^+ \\ \mathbf{E}_1^- \end{pmatrix} = \mathbb{M} \begin{pmatrix} \mathbf{E}_2^+ \\ \mathbf{E}_2^- \end{pmatrix} = \prod_{i=1}^{n} \mathbb{M}_{\text{layer}}^{(i)} \begin{pmatrix} \mathbf{E}_2^+ \\ \mathbf{E}_2^- \end{pmatrix}, \tag{4}$$

where $\mathbb{M}_{\text{layer}}^{(i)}$ is the wave matrix for the ith metasurface layer, including the patterned metallic cladding and supporting dielectric substrate [Fig. 1(b)]. For a patterned metallic cladding having only an electric response, the individual response is characterized by its 2×2 electric sheet admittance $\mathbf{Y}_i$. To describe propagation through the ith layer (Fig. 1), we denote by $\mathbf{T}_i$ the 2×2 transmission matrix for the material interface, by η_i the incident wave impedance on the patterned metallic cladding, and by $\Phi_i = e^{j\phi_i}\mathbf{I}$ the propagation phase delay across the dielectric substrate. The wave matrices can then be expressed in terms of $\mathbf{Y}_i$ as [28]

$$\mathbb{M}_{\text{layer}}^{(i)} = \left(\mathbf{T}_i \otimes \mathbf{I} + \frac{\eta_i}{2}\mathbf{e} \otimes \mathbf{Y}_i\right)(\Phi_i \otimes \mathbf{I}), \tag{5}$$

where $\mathbf{e} = \left(\begin{smallmatrix} 1 & 1 \\ -1 & -1 \end{smallmatrix}\right)$ and $\otimes$ denotes the Kronecker tensor product. Equation (5) can be directly solved for the complex tensor sheet admittance $\mathbf{Y}_i$ of each layer, given the desired S parameters [28]. To possess the degrees of freedom necessary for arbitrary wave transformations, at least three layers are required. For the $n = 3$ case, the center-layer sheet admittance $\mathbf{Y}_2$ can be directly calculated based on the wave matrices and used to obtain the remaining admittances $\mathbf{Y}_1$ and $\mathbf{Y}_3$ (see the Appendix) [28]. For the $n > 3$ case, the sheet admittances of the center layers possess additional degrees of freedom that enable the design to be further optimized for other performance dimensions, such as bandwidth and robustness to fabrication imperfections.

For the case in which the incident wave has TE polarization, the wave-matrix description of the cascaded metasurface simplifies to a loaded transmission-line model [18,25,31]. This analysis also works for TM waves. In this model, the incident and transmitted transverse-wave impedances correspond to the input and output impedances of the transmission line network, while the scalar electric sheet admittances act as shunt loads. In addition, the dielectric spacers are equivalent to interconnection using a lossless transmission line with characteristic wave impedance η_d (see the Appendix). Assuming plane-wave illumination on the unit cell, for $n = 3$ layers [18,31], the scalar sheet admittance Y_i for each layer resulting in a reflectionless transmission can be obtained from this model as follows:

$$\begin{aligned} Y_2 &= \frac{B - j\,\sin(2\phi_d)\eta_d}{-\sin^2(\phi_d)\eta_d^2}, \\ Y_1 &= \frac{D - \cos(2\phi_d) - j\,\sin(2\phi_d)\eta_d Y_2/2}{j\,\sin(2\phi_d)\eta_d - \sin^2(\phi_d)\eta_d^2 Y_2}, \\ Y_3 &= \frac{A - \cos(2\phi_d) - j\,\sin(2\phi_d)\eta_d Y_2/2}{j\,\sin(2\phi_d)\eta_d - \sin^2(\phi_d)\eta_d^2 Y_2}, \end{aligned} \tag{6}$$

where $\phi_d = \phi_1 = \phi_2$ is the propagation phase delay across the dielectric substrate between the sheet admittances. The parameters A, B, and D are defined as

$$\begin{aligned} A &= \cos\varphi\sqrt{\eta_1/\eta_2}, \\ B &= -j\,\sin\varphi\sqrt{\eta_1\eta_2}, \\ D &= \cos\varphi\sqrt{\eta_2/\eta_1}, \end{aligned} \tag{7}$$

where φ is the desired transmission phase shift in Eq. (2) (for details, see the Appendix). These expressions allow the patterned metallic claddings of the metasurface to be individually engineered to realize the prescribed sheet admittances and then cascaded to synthesize the desired scattering parameters.

B. Antireflection and wavefront manipulation

To evaluate the antireflection capabilities of the designed metasurfaces, we perform numerical simulations using an interface between air and a lossless dielectric material with relative permittivity ε_2. The metasurfaces comprise three patterned metallic claddings and three dielectric spacers with dielectric permittivity $\varepsilon_d = 4.2$ (for FR4 microwave substrate) and an overall thickness of $\lambda/80$ ($\lambda/200$ for the spacing layers and $\lambda/400$ for the outermost layer, which is added to facilitate experimental characterization). Figure 2(a) shows the sheet admittances prescribed by Eq. (4) to realize antireflection for a normally incident plane wave for ε_2 ranging from 1 to 80 and φ from 0 to 2π. These sheet admittances are purely imaginary and therefore can be realized using low-loss passive structures. The ideal sheet admittances are modeled as equivalent surface current densities ($J_s = E_y Y_i$) in the commercial electromagnetics solver COMSOL Multiphysics. The full-wave simulations demonstrate nearly perfect antireflection for $\varepsilon_2 = 10$, 40, and 70, with the phase shift arbitrarily fixed to $\varphi = \pi/3$ [Fig. 2(b)]. The phase shift is fully controllable from 0 to 2π, as shown by the full-wave simulations in Fig. 2(c) for $\varepsilon_2 = 78$.

We next illustrate wavefront manipulation capabilities by focusing the normally incident plane wave into different materials without reflection. For an infinite aperture, the required phase profile is given by

$$\varphi(x) = -\frac{2\pi\sqrt{\varepsilon_2}}{\lambda}\left(\sqrt{x^2 + f^2} - f\right) + \varphi_0, \tag{8}$$

where φ_0 is a constant phase shift imposed on all cells and f is the desired focal length. Due to the finite aperture of the metasurface, f should be selected to account for the slight shift in the maximum-intensity point toward the interface [32] (see the Appendix). We quantify the transmission and wavefront manipulation capabilities of the metasurface using the transmission and focusing efficiencies. The transmission efficiency is defined as the fraction of power transmitted through the metasurface, which is obtained by integrating the power density over the aperture

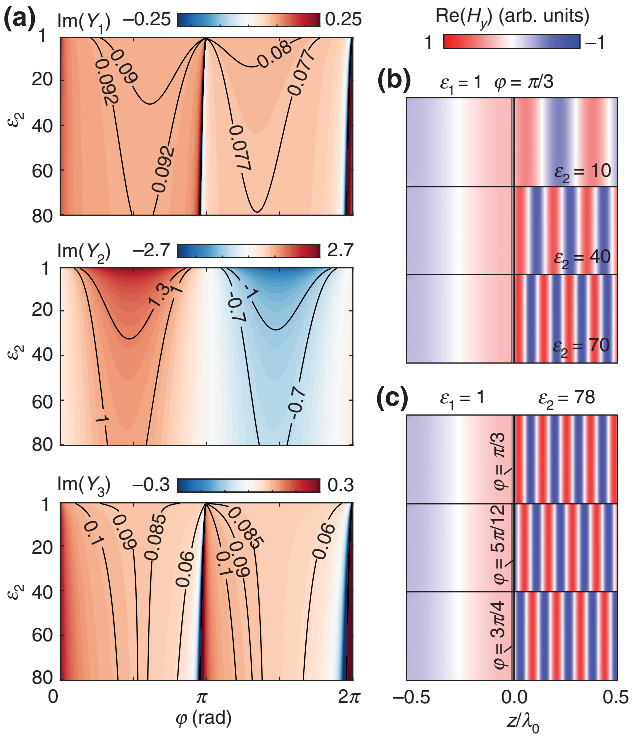

FIG. 2. Antireflection from air into dielectric media. (a) The calculated sheet admittances $\mathrm{Im}(Y_i)$ for antireflection of a normally incident plane wave into media with relative permittivity ε_2 and a phase change φ. The admittances are all purely imaginary. (b),(c) Full-wave simulations of the magnetic field transmitted from air into media with (b) constant phase change $\varphi = \pi/3$ and $\varepsilon_2 = 10$, 40, and 70 (top to bottom) and (c) $\varepsilon_2 = 78$ and phase changes $\varphi = \pi/3$, $5\pi/12$, and $3\pi/4$ (top to bottom).

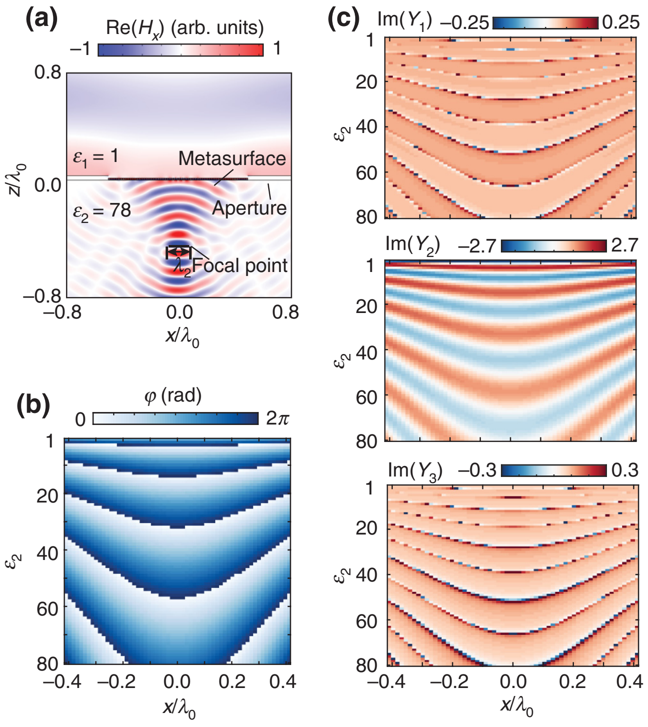

FIG. 3. Wavefront manipulation using a metasurface that focuses a normal incident plane wave from air into different media (from $\varepsilon_2 = 1$ to $\varepsilon_2 = 80$) at 5-cm ($\lambda/2.5$) depth. The metasurface, having a total length of 10.4 cm (0.83λ), is evenly divided into 60 unit cells along the x axis. (a) An example of the magnetic field for a metasurface that focuses a normal incident plane wave from air into water ($\varepsilon_2 = 78$). (b) The phase change across the metasurface as a function of its location. (c) The sheet admittances of the metasurface for focusing.

of the metasurface in the second medium. The focusing efficiency is defined as the fraction of power focused to a $\lambda/(2\sqrt{\varepsilon_2})$ spot (0.71-cm radius in water) at the designed focal depth.

Figure 3(a) shows an illustrative example using a metasurface consisting of 60 equally spaced unit cells, spanning a length of 10.4 cm (0.83λ) in the x direction. A normally incident $\hat{y}$-polarized plane wave is focused into water ($\varepsilon_2 = 78$) at 5-cm ($\lambda/2.5$) depth with a transmission efficiency of 98.7% and a focusing efficiency of 87.5% [33]. For comparison, only 5.5% of the incident power is transmitted to the focal spot in the absence of the metasurface. The performance of the metasurface closely agrees with analytical expressions for the focusing efficiency using a continuous phase profile and a finite aperture, which yields a maximum focusing efficiency of 89.3% [32]. The parabolic phase profiles required to focus the incident wave into a material with $\varepsilon_2 = 1$–80 are shown in Fig. 3(b). These phase profiles can all be realized with purely imaginary (reactive) sheet admittances [Fig. 3(c)] to achieve both antireflection and wavefront focusing.

C. Unit-cell structure

The metasurface layers can be realized using either an interdigitated capacitor structure for a capacitive admittance $\mathrm{Im}(Y_i) > 0$ or an H-shaped structure for an inductive admittance $\mathrm{Im}(Y_i) < 0$ (for guidelines on the structure design, see the Appendix). To extract the admittance of the structure, scattering from a single layer is simulated using the commercial solver COMSOL Multiphysics. The sheet admittance is related to the scattering parameters as [10]

$$\mathbf{Y} = \left(\frac{\mathbf{I} - \mathbf{S}_{11}}{\eta_{\mathrm{in}}} - \frac{\mathbf{I} + \mathbf{S}_{11}}{\eta_{\mathrm{tr}}}\right)(\mathbf{I} + \mathbf{S}_{11})^{-1}, \tag{9}$$

where η_{in} and η_{tr} are the incident and transmit wave impedance, respectively. An important design consideration from Eq. (9) is that the admittance of the sheet depends on the surrounding media. To mitigate this effect, the last layer of the metasurface may incorporate a known dielectric substrate to act as a spacer from the environment. Each unit cell is designed individually using numerical simulations with the local periodicity approximations [29,34,35].

III. RESULTS

A. Reflectionless transmission between air and glass

We first demonstrate the reflectionless transmission of a planar wavefront at 2.4 GHz. The metasurface operates as an antireflection coating with deeply subwavelength thickness when placed at the interface between air ($\varepsilon_1 = 1$) and tempered glass ($\varepsilon_2 = 6.5$), which can be applied to enhance the transmission of wireless signals through windows. To begin the design, we set the dimensions of the unit cell to 6 mm × 6 mm ($\lambda/20.8 \times \lambda/20.8$), with a thickness of 5 mm ($\lambda/25$). The thickness of the dielectric ($\varepsilon_d = 4.2$ for FR4 substrate) between two sequential metallic claddings is set to 2 mm and the thickness of the last dielectric spacer to 1 mm [Fig. 4(a)]. The phase change is set to $\varphi = 1.04\pi$ to minimize the sheet admittance values for the three layers [Fig. 2(a)], resulting in the design values $Y_1 = 0.0193j\ \Omega^{-1}$, $Y_2 = 0.0107j\ \Omega^{-1}$, and $Y_3 = 0.0356j\ \Omega^{-1}$.

Figures 4(b)–4(d) show the designed metallic patterns consisting of interdigitated capacitor structures. For a normally incident $\hat{y}$-polarized plane wave, the capacitive response mainly depends on the gap g, with smaller values of g yielding a larger capacitance [Fig. 4(b)]. The capacitive response can also be increased by increasing the total finger number N, the finger length l, and the finger width h. However, the maximum values of these design parameters are limited by the size of the unit cell and fabrication tolerances. The metasurface comprising 35 × 35 unit cells is designed with a minimum feature size of 0.01 mm and is fabricated using a commercial multilayer printed-circuit-board process [Fig. 4(e)].

We perform transmission experiments using two panel antennas (Itelite, PAT2409) placed 42 cm (3.4λ) apart in an anechoic chamber. The experimental setup using a vector-network analyzer (Keysight Technologies, FieldFox Handheld Analyzers N9915A) is shown in Fig. 4(f). The transmit antenna, operating at 2.4 GHz, has a beam width of 60° and a dimension of 9.3 cm × 9.3 cm, which gives a far-field distance of 13.8 cm. The antenna is placed at a far-field distance of 19 cm (1.5λ) from the metasurface such that the incident wave can be approximated by a normal plane wave. The transmission between the antenna ports is measured through a square glass slab (3 cm thick, 30 cm side) with two identical metasurfaces placed on opposite sides of the glass slab. To eliminate edge diffraction, the metasurface is placed in a square aperture on a large metallic screen that covers the

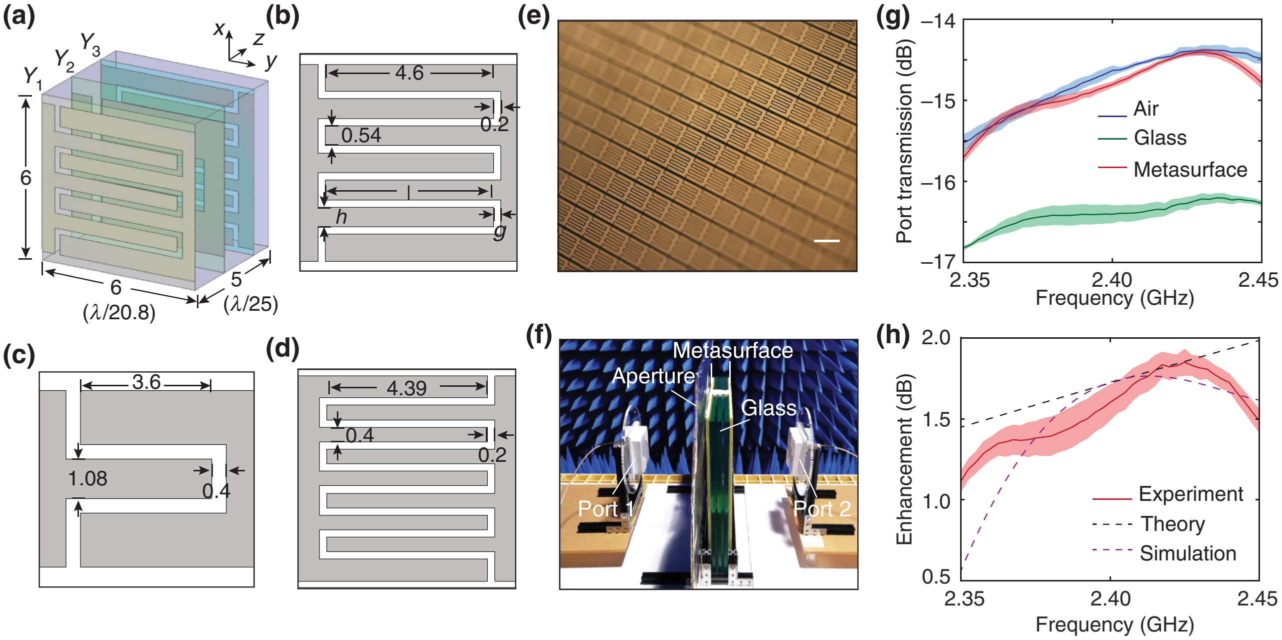

FIG. 4. Wave impedance matching between air and glass. (a) A perspective view of the unit cell. The substrate is made of FR4 ($\varepsilon_2 = 4.2$). The thickness of the substrate between two metallic patterns is 2 mm and that of the outermost substrate is 1 mm. The cell size is $6 \times 6 \times 5$ mm^3. (b)–(d) The structures and dimensions of each impedance sheet: (b) the first sheet, $Y_1 = 0.0193j\ \Omega^{-1}$; (c) the second sheet, $Y_2 = 0.0107j\ \Omega^{-1}$; (d) the third sheet, $Y_3 = 0.0356j\ \Omega^{-1}$. All units are in millimeters. (e) A photograph of the fabricated metasurface: scale bars 6 mm. (f) An image of the experimental setup. (g) The experimentally measured transmission between two panel antennas in air, with a 3-cm-thick glass placed in the center and having metasurfaces on the two surfaces of the glass as shown in (f). The graphs show the mean ± s.d. ($n = 3$ technical trials). (h) The enhancement in transmission between the antennas obstructed by the glass slab, for the case in which the metasurfaces are placed on the glass slab. The theoretical calculations are based on Fabry-Perot resonance and the numerical simulations use an infinite periodic structure.

surface of the glass on the side illuminated by the transmit antenna.

We verify the measured transmission against a theoretical model of transmission through a Fabry-Perot resonator. For a plane wave normally incident on a lossless slab, the effective transmission through the slab is

$$T_{\text{eff}} = \frac{(1-r_{12})^2}{(1-r_{12})^2 + 4r_{12}^2 \sin^2(2\pi\sqrt{\varepsilon_2}d/\lambda)}, \tag{10}$$

where ε_2 is the relative permittivity of glass, d is the glass thickness, and $r_{12} = (\sqrt{\varepsilon_2} - \sqrt{\varepsilon_1})/(\sqrt{\varepsilon_1} + \sqrt{\varepsilon_2})$ is the reflection coefficient. For comparison, we also perform full-wave simulations using periodic boundary conditions of a single unit cell to model the frequency response of the structure. Figure 4(g) shows the experimentally measured transmission between the antenna ports. At 2.4 GHz, the presence of the glass slab decreases transmission by about 1.7 dB compared to no obstruction between the two antennas, whereas placing a metasurface on each side of the slab restores the transmission to that without the glass slab. Comparison of the enhancement in transmission with Eq. (10) and simulations shows that the results are in good agreement at the design frequency of 2.4 GHz, although the experimental and simulation curves deviate away from the design frequency due to dispersion of the metasurface [Fig. 4(h)].

B. Microwave focusing from air into water

We next demonstrate the ability of the cascaded metasurface to focus a normally incident plane wave from air into water ($\varepsilon_2 = 78$) without reflection. This functionality is important for technologies ranging from underwater communications to wireless power transfer for biomedical implants. For simplicity, we consider a scalar generalization of the metasurface design to three dimensions by repeating the unit cell designed for two-dimensional

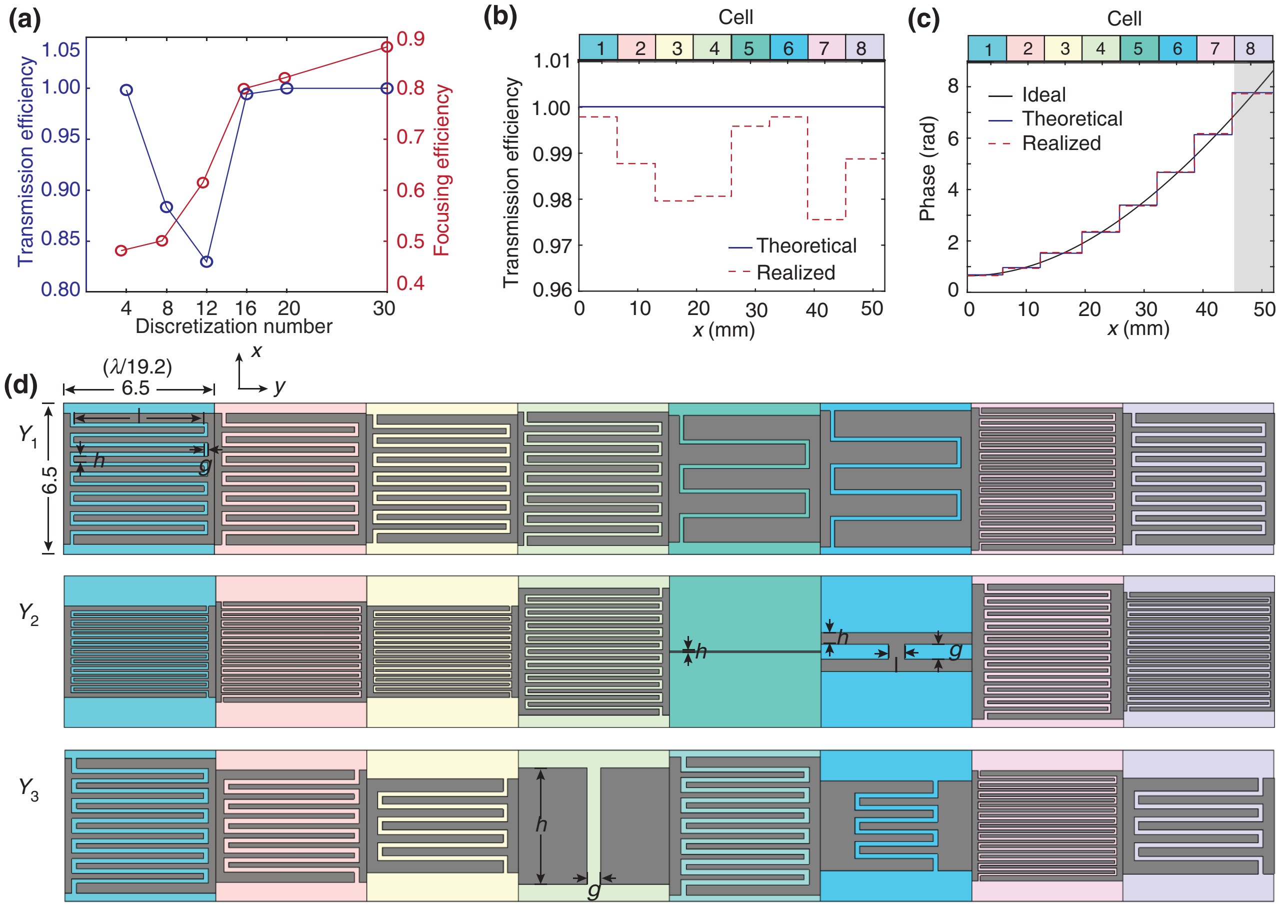

FIG. 5. The unit-cell design of the antireflection metasurface focusing a normal incident plane wave from air into water at 5-cm ($\lambda/2.5$) depth. (a) A discretization study of the transmission and focusing efficiency as a function of the number of unit cells with $\varphi_0 = 0$. (b),(c) The theoretical designed and physically realized (b) transmission efficiency and (c) phase changes for the eight unit cells. The shaded region area shows the area for 2π phase wrap. (d) The geometry of the unit cells from cell 1 to cell 8 (left to right) and from sheet 1 to sheet 3 (top to bottom), respectively: the units are millimeters. The corresponding sheet admittances and specific dimensions for each cell are stated in Tables I and II, respectively. The water is simulated with a relative permittivity of $\varepsilon_2 = 78$.

TABLE I. The metasurface sheet admittances for reflectionless focusing of a normally incident plane wave from air into water. The focal depth is 5 cm ($\lambda/2.5$) and the unit-cell size is 6.5×6.5 mm^2. Unit cells are numbered from center to edge. Sheet admittance Y_i unit: Ω^{-1}.

Sheet	Cell 1	Cell 2	Cell 3	Cell 4	Cell 5	Cell 6	Cell 7	Cell 8
Y_1	0.0352j	0.0337j	0.0326j	0.0381j	0.0185j	0.0181j	0.0645j	0.0315j
Y_2	0.1406j	0.1493j	0.1446j	0.0896j	−0.013j	−0.0501j	0.0781j	0.1651j
Y_3	0.0514j	0.0445j	0.0335j	0.0040j	0.0458j	0.0190j	0.1333j	0.0329j

focusing of a TE-polarized wave in a concentric manner. This approximation implements the phase profile in Eq. (8), with the position coordinate x replaced by the radial distance $u = \sqrt{x^2 + y^2}$, neglecting the difference in wave impedances emerging from the TM-polarized wave components in three dimensions.

We set the diameter of the metasurface to 104 mm ($\lambda/1.2$) and the thickness to 5 mm ($\lambda/25$), specifying the focal length to be 5 cm ($\lambda/2.5$) from the air-water interface. The discretization of the metasurface is first studied by evaluating the transmission and focusing efficiency of a two-dimensional metasurface using ideal sheet admittances with the global phase parameter $\varphi_0 = 0$. As shown in Fig. 5(a), the focusing efficiency is above 80% when the number of unit cells is greater than 16 and the transmission efficiencies remain above 80% even when only four unit cells are used. In comparison, the transmission efficiency is 31.7% without the metasurface. We set the number of unit cells to 16 for ease of fabrication, resulting in cell dimensions of 6.5 mm × 6.5 mm ($\lambda/19.2 \times \lambda/19.2$). The discretization is also sufficient to ensure that the phase difference between any two adjacent cells is no larger than $\pi/2$. Owing to the symmetry of the focusing configuration, the design requires only eight unique unit cells.

The designs of the metallic patterns for each layer of the unit cells are shown in Fig. 5(d). The unit cells implement the sheet admittances given in Table I, which are obtained using a global phase parameter of $\varphi_0 = 0.21\pi$ to minimize the capacitive admittances and inductive impedance of the layers. The required sheet admittances are primarily capacitive and are realized using an interdigitated capacitor structure, although two elements require an inductive response that can be realized by using a straight metallic trace or the H-shaped structure (specific dimensions in Table II). Numerical simulations of the individual unit cells with periodic boundary conditions show that the designs all achieve a transmission efficiency greater than 97% [Fig. 5(b)] and realize a phase shift φ that is in close agreement with the design value [Fig. 5(c)]. In addition, the effect for oblique incidence is negligible for an angle smaller than 30° [33].

Figure 6(a) shows the metasurface for three-dimensional (3D) focusing obtained by arranging the unit cells in a concentric circular geometry. We fabricate the metasurface using a commercial multilayer printed-circuit-board process comprising copper on FR4 substrate [Fig. 6(b)]. To experimentally validate the microwave focusing, we place the metasurface on the wall of a large rectangular acrylic container (width 45 cm, height 30 cm, length 50 cm, and wall thickness 5 mm) filled with water. The container wall is factored into the design by adding its thickness to the dielectric substrate, since acrylic has a relatively similar dielectric permittivity to FR4. To eliminate edge diffraction, the surface of the container is covered with a metallic screen with a 5.7-cm-radius aperture opened for the metasurface. A transmitting panel antenna illuminates the metasurface at a distance of 17 cm (1.36λ) in air, as

TABLE II. The unit-cell dimensions for the metasurface focusing a normally incident plane wave from air into water. Units: millimeters.

Sheet	Parameters	Cell 1	Cell 2	Cell 3	Cell 4	Cell 5	Cell 6	Cell 7	Cell 8
Y_1	N	13	13	13	13	5	5	2	13
	l	5.55	5.54	5.55	5.63	5.35	5.27	5.65	5.39
	g	0.17	0.17	0.18	0.14	0.18	0.18	0.10	0.18
	h	0.25	0.25	0.23	0.29	1.00	0.95	0.14	0.24
Y_2	N	19	21	19	19	–	–	21	25
	l	5.70	5.70	5.74	5.64	–	0.70	5.13	5.95
	g	0.10	0.10	0.10	0.12	–	0.66	0.13	0.10
	h	0.10	0.10	0.10	0.16	0.08	0.50	0.14	0.10
Y_3	N	13	11	7	2	13	7	21	7
	l	5.47	5.41	5.20	–	5.22	3.16	5.77	5.14
	g	0.20	0.21	0.20	0.57	0.22	0.20	0.10	0.20
	h	0.23	0.21	0.35	5.00	0.22	0.32	0.12	0.36

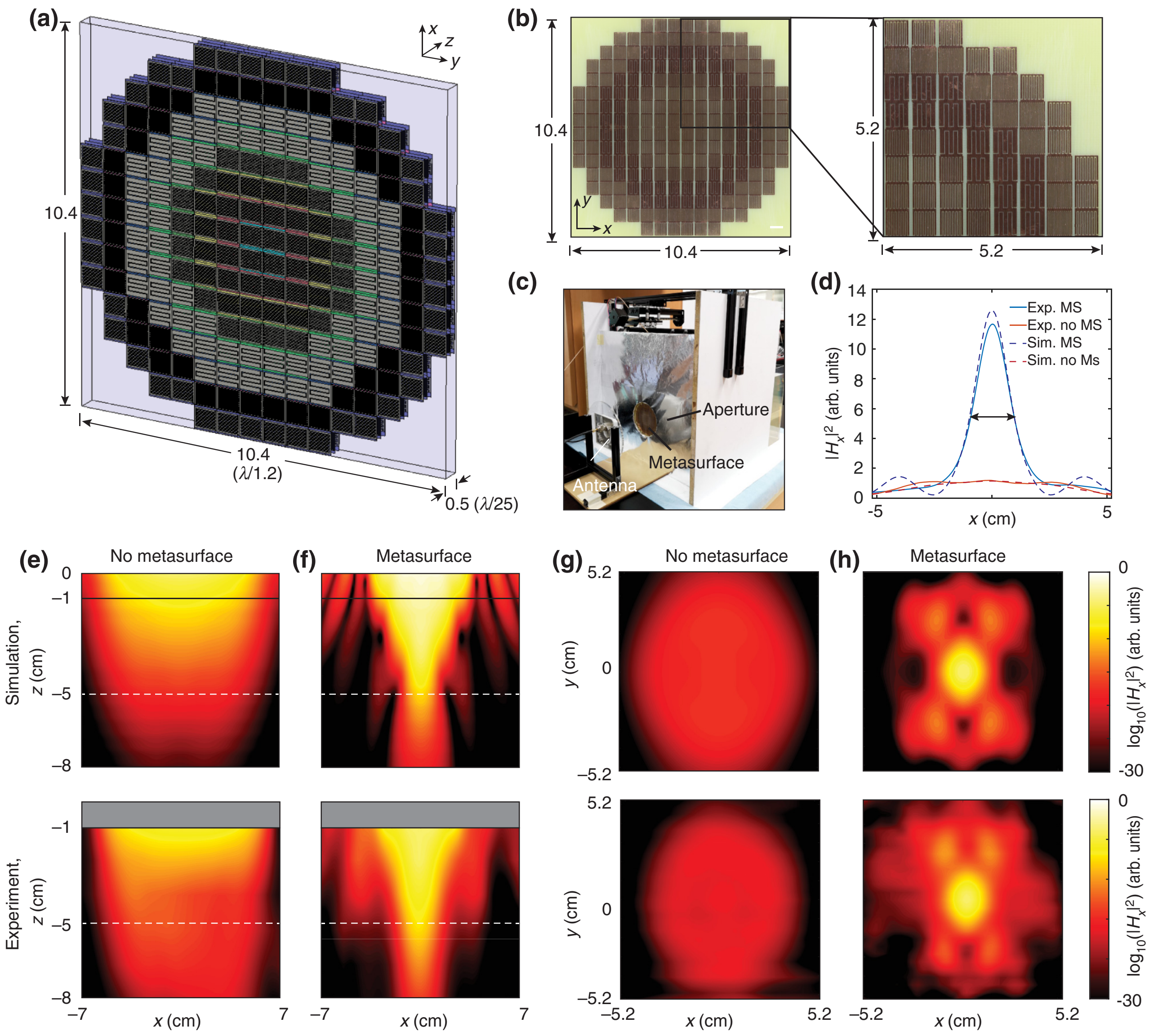

FIG. 6. Antireflection focusing from air into 5-cm ($\lambda/2.5$) depth in water. (a) A perspective view of the metasurface using eight unit cells distributed in a circular ring form. Cells occupying the same background color are identical. (b) A photograph of the fabricated metasurface: a quarter of the metasurface is enlarged on the right. (c) A photograph of the experimental setup. (d) The normalized magnetic field intensity along the focusing depth with and without the metasurface (MS) from simulation (Sim.) and experiment (Exp.). The arrow indicates the full width at half maximum (FWHM) of 0.16λ. (e),(f) The simulated (top) and measured (bottom) magnetic field intensity at the x-z plane (e) without and (f) with the metasurface. (g),(h) The simulated (top) and measured (bottom) magnetic field intensity at the 5-cm-deep focal plane (x-y plane) (g) without and (h) with the metasurface. The water is simulated with a complex relative permittivity $\varepsilon_2 = 78 - 11.7j$.

shown in Fig. 6(c). To map the transmitted field, a magnetic probe (Langer EMW-Technik, RF R 0,3-3) is scanned through the water container using a two-axis positioner (HANPOSE, 17HS3401S) and the received power is measured using a spectrum analyzer (Keysight CXA Signal Analyzer).

To provide insight, we compare the measurements with full-wave simulations of the metasurface in the 3D focusing configuration using plane-wave illumination and water ($\varepsilon_2 = 78 - 11.7j$). The field profile at the focal spot 5 cm from the air-water interface is shown in Fig. 6(d). The measured width of the focal spot is about 2 cm (0.16λ) FWHM, which is in close agreement with the 3D simulation. To estimate the reflection from the metasurface, we compare the field intensity at the focal plane with and without the metasurface. In both simulation and experiment, the enhancement at the focal spot is nearly 12 times compared to the aperture without the metasurface. The transmission efficiency, defined as the fraction of power transmitted through the metasurface, is therefore comparable to that in the simulation, which is about 67.8% compared to 46.6% at the air-water interface without the metasurface [33]. Figures 6(e)–6(h) show the simulated and experimentally measured field intensities in the transverse and focal planes. Due to the scalar approximation of 3D focusing, the focal spot exhibits broadening in the y direction, where the TM-polarized wave components are most significant. Although the metasurface provides the correct phase shift for focusing regardless of incident polarization, TM-wave transmission is reduced as a result of imperfect transverse-wave impedance matching.

IV. DISCUSSION AND CONCLUSIONS

We systematically design and experimentally demonstrate cascaded metasurfaces with a deeply subwavelength thickness for antireflection and wavefront manipulation. The versatility of this class of metasurfaces and their application to radio-frequency technologies are illustrated by demonstrating near-perfect transmission through the glass and near-reflectionless focusing into the water at wireless communication frequencies (2.4 GHz). Such antireflection metasurfaces, which can be designed for other common building materials, could enable wireless signals (such as Wi-Fi) to transmit through indoor obstacles without reflection to enhance connectivity. The metasurface thickness can be further reduced by using smaller-sized unit cells in order to eliminate the interaction between adjacent layers, although this may increase the difficulty in designing metallic patterns to realize the sheet admittances. The thinness of the metasurfaces may facilitate flexible designs that can be interfaced with the body to mitigate reflection and focus energy for biomedical applications in wireless sensing or power transfer. These results provide a general approach to control electromagnetic waves at interfaces between different materials in the long-wavelength regime.

Future work may extend the analysis of the metasurface to nonplanar boundaries to facilitate the development of conformal metasurfaces [36]. Investigation of the robustness of the metasurface to shape deformations may further enable soft and flexible metasurfaces for applications in wearable devices and robotics [37]. Wave impedance matching and wavefront control for circularly polarized waves could be explored to make the receiver inside the body independent of the orientation. Dynamic functionalities may also be integrated through the incorporation of variable electronic components into the unit-cell structure of the metasurface to adaptively control reflection and propagation at the interface [38]. The cascaded metasurfaces may also have applications in photonics for realizing subwavelength components that control optical transmission between silicon and free space. They could also enhance a broad range of polarimetric and spectroscopic techniques for analysis of chemical and biological media [39,40].

ACKNOWLEDGMENTS

J.S.H. acknowledges support from the National Research Foundation Singapore (Grant No. NRF-NRFF2017-07) and the Ministry of Education Singapore (Grants No. MOE2016-T2-2-016 and No. MOE2016-T3-1-004). A.G. and B.O.R. acknowledge support by a National Science Foundation (NSF) Graduate Research Fellowship under Grant No. DGE 1256260 and the Office of Naval Research under Grant No. NOOO14-18-1-2536.

APPENDIX

1. Solution for the wave-matrix model

The wave-matrix formalism below follows that in Ref. [28]. For robustness of the design, an additional dielectric layer is added after the last metallic pattern to act as a spacer from the second medium. To account for this space, the last wave matrix $\mathbb{M}_{\text{layer}}^{(n)}$ is modified to include the effect of the additional dielectric layer as

$$\mathbb{M}_{\text{layer}}^{(n)} = \left(\mathbf{T}_n \otimes \mathbf{I} + \frac{\eta_n}{2}\mathbf{e} \otimes \mathbf{Y}_n\right)(\Phi_n \otimes \mathbf{I})(\mathbf{T}_{n+1} \otimes \mathbf{I}), \tag{A1}$$

where $\mathbf{T}_{n+1}$ is the transmission matrix for the interface between the dielectric layer and the second medium.

The transmission matrix at the ith interface is defined as $\mathbf{T}_i = (1/t)\left(\begin{smallmatrix} 1 & r \\ r & 1 \end{smallmatrix}\right)$, where r and t are the Fresnel reflection and transmission coefficients across the interface, respectively. Equation (4) for the $n = 3$ case can be rewritten as

$$\begin{aligned}\mathbb{M} = {} & \left(\mathbf{T}_1 \otimes \mathbf{I} + \frac{\eta_1}{2}\mathbf{e} \otimes \mathbf{Y}_1\right)(\Phi_1 \otimes \mathbf{I})\left(\mathbf{T}_2 \otimes \mathbf{I} + \frac{\eta_d}{2}\mathbf{e} \otimes \mathbf{Y}_2\right) \\ & (\Phi_2 \otimes \mathbf{I})\left(\mathbf{T}_3 \otimes \mathbf{I} + \frac{\eta_d}{2}\mathbf{e} \otimes \mathbf{Y}_3\right)(\Phi_3 \otimes \mathbf{I})(\mathbf{T}_4 \otimes \mathbf{I}).\end{aligned} \tag{A2}$$

The sheet impedance is solved as follows:

$$\begin{aligned}\mathbf{e} \otimes \mathbf{Y}_1 = \frac{1}{a_1}\Big[& \mathbb{M}(\Phi_3\mathbf{T}_4 \otimes \mathbf{I})^{-1}(\mathbf{e} \otimes \mathbf{I}) \\ & - (\mathbf{T}_1\Phi_1\mathbf{T}_2\Phi_2\mathbf{T}_3\mathbf{e}) \otimes \mathbf{I} - \\ & \frac{\eta_d}{2}(\mathbf{T}_1\Phi_1\mathbf{e}\Phi_2\mathbf{T}_3\mathbf{e}) \otimes \mathbf{Y}_2\Big] \\ & \times \left[\mathbf{I} \otimes \left(\mathbf{I} + \frac{a_{12}}{a_1}\mathbf{Y}_2\right)^{-1}\right]\end{aligned} \tag{A3}$$

where $a_1\mathbf{e} = \eta_1(\mathbf{e}\Phi_1\mathbf{T}_2\Phi_2\mathbf{T}_3\mathbf{e})/2$ and $a_{12}\mathbf{e} = \eta_1\eta_d(\mathbf{e}\Phi_1\mathbf{e}\Phi_2\mathbf{T}_3\mathbf{e})/4$;

$$\mathbf{e}\otimes\mathbf{Y}_2 = \frac{1}{a_2}\Big[(\mathbf{e}\otimes\mathbf{I})\mathbb{M}(\Phi_3\mathbf{T}_4\otimes\mathbf{I})^{-1}(\mathbf{e}\otimes\mathbf{I}) - (\mathbf{e}\mathbf{T}_1\Phi_1\mathbf{T}_2\Phi_2\mathbf{T}_3\mathbf{e})\otimes\mathbf{I}\Big] \tag{A4}$$

where $a_2\mathbf{e} = \eta_d(\mathbf{e}\mathbf{T}_1\Phi_1\mathbf{e}\Phi_2\mathbf{T}_3\mathbf{e})/2$; and

$$\begin{aligned}\mathbf{e}\otimes\mathbf{Y}_3 = \frac{1}{a_3}&\left[\mathbf{I}\otimes\left(\mathbf{I}+\frac{a_{23}}{a_3}\mathbf{Y}_2\right)^{-1}\right]\\ &\times\Big[(\mathbf{e}\otimes\mathbf{I})\mathbb{M}(\Phi_3\mathbf{T}_4\otimes\mathbf{I})^{-1}\\ &-(\mathbf{e}\mathbf{T}_1\Phi_1\mathbf{T}_2\Phi_2\mathbf{T}_3)\otimes\mathbf{I}\\ &-\frac{\eta_d}{2}(\mathbf{e}\mathbf{T}_1\Phi_1\mathbf{e}\Phi_2\mathbf{T}_3)\otimes\mathbf{Y}_2\Big]\end{aligned} \tag{A5}$$

where $a_3\mathbf{e} = \eta_d(\mathbf{e}\mathbf{T}_1\Phi_1\mathbf{T}_2\Phi_2\mathbf{e})/2$ and $a_{23}\mathbf{e} = \eta_d^2(\mathbf{e}\mathbf{T}_1\Phi_1\mathbf{e}\Phi_2\mathbf{e})/4$.

2. Solution for the transmission line model

The transfer matrix (ABCD) relates the field in different regions and can be converted to the wave matrix $\mathbb{M}$ through the wave impedance as [28]

$$\begin{pmatrix}\mathbf{A} & \mathbf{B}\\ \mathbf{C} & \mathbf{D}\end{pmatrix} = \frac{1}{2}\begin{pmatrix}\mathbf{I} & \mathbf{I}\\ \mathbf{n}/\eta_1 & -\mathbf{n}/\eta_1\end{pmatrix}\mathbb{M}\begin{pmatrix}\mathbf{I} & -\eta_2\mathbf{n}\\ \mathbf{I} & \eta_2\mathbf{n}\end{pmatrix}, \tag{A6}$$

where $\mathbf{n} = \left(\begin{smallmatrix}0 & -1\\ 1 & 0\end{smallmatrix}\right)$ is the matrix for 90° rotation. If only TE or TM waves are considered, the vector matrices are reduced to scalar forms. The transfer matrix models the cascaded metasurface as a transmission line. We have

$$\begin{pmatrix}A & B\\ C & D\end{pmatrix} = \begin{pmatrix}\cos\varphi\sqrt{\eta_1/\eta_2} & -j\sin\varphi\sqrt{\eta_1\eta_2}\\ -j\sin\varphi/\sqrt{\eta_1\eta_2} & \cos\varphi\sqrt{\eta_2/\eta_1}\end{pmatrix}. \tag{A7}$$

For a cascaded metasurface with n sheets (containing n patterned metallic claddings and n dielectric spacers), the transfer matrix is given by

$$\begin{pmatrix}A & B\\ C & D\end{pmatrix} = \prod_{i=1}^{n}\begin{pmatrix}1 & 0\\ Y_i & 1\end{pmatrix}\begin{pmatrix}\cos\phi_i & j\eta_d\sin\phi_i\\ j\sin\phi_i/\eta_d & \cos\phi_i\end{pmatrix}, \tag{A8}$$

where $\left(\begin{smallmatrix}1 & 0\\ Y_i & 1\end{smallmatrix}\right)$ represents the patterned metallic sheet response of the ith layer, and $\left(\begin{smallmatrix}\cos\phi_i & j\eta_d\sin\phi_i\\ j\sin\phi_i/\eta_d & \cos\phi_i\end{smallmatrix}\right)$ is the wave propagation through the dielectric spacer. The phase delay ϕ_i within the ith dielectric spacer depends on its relative permittivity ε_d and thickness d_i, that is, $\phi_i = 2\pi\sqrt{\varepsilon_d}d_i/\lambda$.

When $n = 3$ and the dielectric spacers between two adjacent metallic sheets are the same ($\phi_1 = \phi_2 = \phi_d$), the sheet impedance can be calculated as

$$\begin{aligned}Y_2 &= \frac{B' - j\sin(2\phi_d)\eta_d}{-\sin^2(\phi_d)\eta_d^2},\\ Y_1 &= \frac{D' - \cos(2\phi_d) - j\sin(2\phi_d)\eta_d Y_2/2}{j\sin(2\phi_d)\eta_d - \sin^2(\phi_d)\eta_d^2 Y_2},\\ Y_3 &= \frac{A' - \cos(2\phi_d) - j\sin(2\phi_d)\eta_d Y_2/2}{j\sin(2\phi_d)\eta_d - \sin^2(\phi_d)\eta_d^2 Y_2},\end{aligned} \tag{A9}$$

where

$$\begin{aligned}A' &= A\cos\phi_3 - jB\sin\phi_3/\eta_d,\\ B' &= B\cos\phi_3 - jA\eta_d\sin\phi_3,\\ D' &= D\cos\phi_3 - jC\eta_d\sin\phi_3.\end{aligned} \tag{A10}$$

3. Unit-cell pattern design

The patterns corresponding to the prescribed sheet admittances are obtained by varying the geometrical parameters of a unit cell. For scalar capacitive admittances, analytical expressions are available to estimate the geometry of the interdigitated capacitor. The surface capacitance C_s is obtained by an analytical model [41] as

$$C_s = \frac{\varepsilon_d K}{1.8\times 10^4\pi}(N-1)l, \tag{A11}$$

where N is the number of interdigital fingers and l is the length of the finger. The parameter K depends on the width h and the gap g of the finger [Fig. 4(b)]. The scalar sheet admittance is then given by $Y = j\omega C_s$, where ω is the operating frequency.

The inductive admittances are obtained through tuning the H-shape-structured metallic pattern [20]. Generally, reducing the length of the center trace g gives larger inductive values [Fig. 5(d)]. The desired inductance can be more precisely tuned through changing the width of the center l and/or the side trace h, which follows the trend that the wider the trace is, the larger are the inductances.

4. Focal shift

When a plane wave is focused by a small aperture, the actual maximum intensity point shifts closer to the aperture due to edge diffraction [32]. The shift becomes significant for an aperture with a Fresnel number smaller than 5. The Fresnel number F is defined as

$$F = \frac{a^2}{f\lambda}, \tag{A12}$$

where a is the radius of the aperture, f is the focal length, and λ is the wavelength. The approximate focal shift Δf

between the focal point and the maximum intensity point for a circular aperture is

$$\Delta f \approx -\frac{f}{1+(\pi^2/12)F^2}, \tag{A13}$$

where the minus sign means that the shift is toward the aperture. For our focusing metasurface, the Fresnel number $F = 2.91$ and the approximate focal shift is 0.82 cm.

[1] H. M. Jol, ed., *Ground Penetrating Radar Theory and Applications* (Elsevier, Amsterdam, 2009).

[2] T. Saarenketo and T. Scullion, Road evaluation with ground penetrating radar, J. Appl. Geophy. **43**, 119 (2000).

[3] F. Yang, P. Mun Lee, Z. Dong, X. Tian, and J. S. Ho, Enhancing Wireless Transmission from the Body with Wearable Diffractive Patterns, Phys. Rev. Appl. **12**, 054020 (2019).

[4] N. Qasem and R. Seager, in *2010 Loughborough Antennas Propagation Conference* (IEEE, Loughborough, UK, 2010), p. 309.

[5] T. Hao, W. Zheng, W. He, and K. Lin, Air-ground impedance matching by depositing metasurfaces for enhanced GPR detection, IEEE Trans. Geosci. Remote Sens. **58**, 4061 (2020).

[6] J. S. Ho, A. J. Yeh, E. Neofytou, S. Kim, Y. Tanabe, B. Patlolla, R. E. Beygui, and A. S. Y. Poon, Wireless power transfer to deep-tissue microimplants, Proc. Natl. Acad. Sci. **111**, 7974 (2014).

[7] J. S. Ho, B. Qiu, Y. Tanabe, A. J. Yeh, S. Fan, and A. S. Y. Poon, Planar immersion lens with metasurfaces, Phys. Rev. B **91**, 125145 (2015).

[8] H. A. MacLeod, *Thin-Film Optical Filters* (CRC Press/Taylor & Francis, Boca Raton, FL, 2010).

[9] N. Yu, P. Genevet, M. A. Kats, F. Aieta, J.-P. Tetienne, F. Capasso, and Z. Gaburro, Light propagation with phase discontinuities: Generalized laws of reflection and refraction, Science **334**, 333 (2011).

[10] C. Pfeiffer, C. Zhang, V. Ray, L. J. Guo, and A. Grbic, High Performance Bianisotropic Metasurfaces: Asymmetric Transmission of Light, Phys. Rev. Lett. **113**, 023902 (2014).

[11] C. Pfeiffer and A. Grbic, Bianisotropic Metasurfaces for Optimal Polarization Control: Analysis and Synthesis, Phys. Rev. Appl. **2**, 044011 (2014).

[12] A. Arbabi, Y. Horie, M. Bagheri, and A. Faraon, Dielectric metasurfaces for complete control of phase and polarization with subwavelength spatial resolution and high transmission, Nat. Nanotechnol. **10**, 937 (2015).

[13] Z. Ze-Peng, C. Rui, F. Zhi-Bin, P. Xiao-Ning, and D. Jian-Wen, High focusing efficiency in subdiffraction focusing metalens, Nanophotonics **8**, 1279 (2019).

[14] Y. Jianing, W. Xiaoyu, S. Jiakun, H. Cheng, H. Yijia, and L. Xiangang, Cascaded metasurface for simultaneous control of transmission and reflection, Opt. Express **27**, 9061 (2019).

[15] H.-T. Chen, J. Zhou, J. F. O'Hara, F. Chen, A. K. Azad, and A. J. Taylor, Antireflection Coating Using Metamaterials and Identification of its Mechanism, Phys. Rev. Lett. **105**, 073901 (2010).

[16] W. A. Zheng and T. Hao, in *2019 Thirteenth International Congress on Artificial Materials for Novel Wave Phenomena (Metamaterials)* (IEEE, Rome, Italy, 2019), p. X–489.

[17] H. Cano-Garcia, P. Kosmas, and E. Kallos, in *2015 9th International Congress on Advanced Electromagnetic Materials in Microwaves and Optics (METAMATERIALS)* (IEEE, Oxford, United Kingdom, 2015), p. 43.

[18] J. P. S. Wong, A. Epstein, and G. V. Eleftheriades, Reflectionless wide-angle refracting metasurfaces, IEEE Antennas Wirel. Propag. Lett. **15**, 1293 (2016).

[19] V. S. Asadchy and S. A. Tretyakov, Bianisotropic metasurfaces: Physics and applications, Nanophotonics **7**, 1069 (2018).

[20] M. Chen, E. Abdo-Sánchez, A. Epstein, and G. V. Eleftheriades, Theory, design, and experimental verification of a reflectionless bianisotropic Huygens' metasurface for wide-angle refraction, Phys. Rev. B **97**, 125433 (2018).

[21] J. K. Gansel, M. Thiel, M. S. Rill, M. Decker, K. Bade, V. Saile, G. von Freymann, S. Linden, and M. Wegener, Gold helix photonic metamaterial as broadband circular polarizer, Science **325**, 1513 (2009).

[22] M. Chen and G. V. Eleftheriades, Omega-bianisotropic wire-loop Huygens' metasurface for reflectionless wide-angle refraction, IEEE Trans. Antennas Propag. **68**, 1477 (2020).

[23] A. Epstein and G. V. Eleftheriades, in *2016 IEEE International Symposium on Antennas and Propagation (APSURSI)* (2016), p. 97.

[24] A. H. Dorrah, M. Chen, and G. V. Eleftheriades, Bianisotropic Huygens' metasurface for wideband impedance matching between two dielectric media, IEEE Trans. Antennas Propag. **66**, 4729 (2018).

[25] A. Epstein and G. V. Eleftheriades, Arbitrary power-conserving field transformations with passive lossless omega-type bianisotropic metasurfaces, IEEE Trans. Antennas Propag. **64**, 3880 (2016).

[26] V. S. Asadchy, M. Albooyeh, S. N. Tcvetkova, A. Díaz-Rubio, Y. Ra'di, and S. A. Tretyakov, Perfect control of reflection and refraction using spatially dispersive metasurfaces, Phys. Rev. B **94**, 075142 (2016).

[27] A. H. Dorrah and G. V. Eleftheriades, Bianisotropic Huygens' metasurface pairs for nonlocal power-conserving wave transformations, IEEE Antennas Wirel. Propag. Lett. **17**, 1788 (2018).

[28] A. Ranjbar and A. Grbic, Analysis and synthesis of cascaded metasurfaces using wave matrices, Phys. Rev. B **95**, 205114 (2017).

[29] C. Pfeiffer and A. Grbic, Cascaded metasurfaces for complete phase and polarization control, Appl. Phys. Lett. **102**, 231116 (2013).

[30] H. Cheng, Z. Liu, S. Chen, and J. Tian, Emergent functionality and controllability in few-layer metasurfaces, Adv. Mater. **27**, 5410 (2015).

[31] B. O. Raeker and A. Grbic, Compound Metaoptics for Amplitude and Phase Control of Wave Fronts, Phys. Rev. Lett. **122**, 113901 (2019).

[32] L. Yajun and W. Emil, Focal shifts in diffracted converging spherical waves, Opt. Commun. **39**, 211 (1981).

[33] See the Supplemental Material at http://link.aps.org/supplemental/10.1103/PhysRevApplied.14.064044 for characterization of the metasurface at varying focal depths, oblique incidence, and different frequencies.

[34] M. A. Al-Joumayly and N. Behdad, Wideband planar microwave lenses using sub-wavelength spatial phase shifters, IEEE Trans. Antennas Propag. **59**, 4542 (2011).

[35] C. Pfeiffer and A. Grbic, Millimeter-wave transmitarrays for wavefront and polarization control, IEEE Trans. Microw. Theory Tech. **61**, 4407 (2013).

[36] K. Wu, P. Coquet, Q. J. Wang, and P. Genevet, Modelling of free-form conformal metasurfaces, Nat. Commun. **9**, 3439 (2018).

[37] S. Walia, C. M. Shah, P. Gutruf, H. Nili, D. R. Chowdhury, W. Withayachumnankul, M. Bhaskaran, and S. Sriram, Flexible metasurfaces and metamaterials: A review of materials and fabrication processes at micro- and nanoscales, Appl. Phys. Rev. **2**, 011303 (2015).

[38] Z. Wu, Y. Ra'di, and A. Grbic, Tunable Metasurfaces: A Polarization Rotator Design, Phys. Rev. X **9**, 11036 (2019).

[39] A. Ranjbar and A. Grbic, Broadband, Multiband, and Multifunctional All-Dielectric Metasurfaces, Phys. Rev. Appl. **11**, 054066 (2019).

[40] D. Rodrigo, A. Tittl, N. Ait-Bouziad, A. John-Herpin, O. Limaj, C. Kelly, D. Yoo, N. J. Wittenberg, S. Hyun Oh, H. A. Lashuel, and H. Altug, Resolving molecule-specific information in dynamic lipid membrane processes with multi-resonant infrared metasurfaces, Nat. Commun. **9**, 2160 (2018).

[41] I. Bahl, *Lumped Elements for RF and Microwave Circuits* (Artech House, Norwood, MA, 2003).